Submitted to

31st International Conference on High Energy Physics, ICHEP02, July 24, 2002, Amsterdam

Abstract: **1010**

Parallel Session **5**

www-h1.desy.de/h1/www/publications/conf/conf_list.html

Measurement of single inclusive high E_T jet cross-sections in photoproduction at HERA

H1 Collaboration

Abstract

Inclusive jet cross-sections for the reaction $e^+p \to jet + X$ for $Q^2 < 1$ GeV^2 and photon-proton energies in the interval $95 \leq W \leq 285$ GeV have been measured using data collected in the years 1996 - 1997 with the H1 detector at HERA. Jets with transverse energies $E_T^{jet} > 21$ GeV in the pseudorapidity range $-1 \leq \eta^{jet} \leq 2.5$ are searched for using the inclusive k_T cluster algorithm in the laboratory frame. Single-differential and multi-differential cross-sections as a function of η^{jet} and E_T^{jet} are compared with NLO QCD calculations using different sets of photon parton density functions as input. The cross-sections are in good agreement with NLO QCD up to the highest measured values of $E_T^{jet} = 75$ GeV.

1 Introduction

At HERA, the collisions of protons with quasi-real photons emitted from the incoming electrons can result in the production of high transverse momentum jets. In leading order (LO) quantum chromodynamics (QCD) two types of process are responsible for these jets. The photon may interact as a pointlike particle with a parton in the proton, in so called direct processes. Alternatively, the photon may develop a hadronic structure, such that a parton in the photon interacts with a parton in the proton, in which case these processes are called resolved. The hadronic final state consists of high E_T partons which fragment into jets with transverse energy E_T^{jet}, which acts as a hard scale allowing perturbative QCD predictions to be made. Additional energy in the event may come from the proton and/or the photon remnant, as well as from possible soft remnant interactions.

At high E_T^{jet}, where non-perturbative effects are less influential, jet cross-sections reflect the underlying parton-parton dynamics of the photon-proton collision. Therefore, E_T^{jet} spectra measurements offer a means of testing the validity of QCD predictions. The proton parton density functions (PDF) being well constrained by F_2^p DIS measurements, pseudorapidity[1] η^{jet} spectra are essentially sensitive to the photon PDF. Measurements of $d\sigma/d\eta^{jet}$ allow the probing of photon structure at higher scales than those reached at e^+e^- colliders and provide complementary information to that obtained from e.g. dijet analysis.

In this paper, measurements of differential jet cross-sections as a function of the jet transverse energy, E_T^{jet}, and pseudorapidity , η^{jet}, for inclusive jet production in photoproduction are presented. The measurements are corrected to the hadron level and compared with next-to-leading order (NLO) calculations including resolved and direct processes and using available NLO photon PDFs. The data were collected with the H1 detector at the HERA collider in 1996 and 1997, in which positrons of energy $27.5\ \mathrm{GeV}$ collided with protons of energy $820\ \mathrm{GeV}$. The total data sample corresponds to an integrated luminosity of $24.1 \pm 0.4\ \mathrm{pb}^{-1}$. The paper is organized as follows. In section 2 the H1 detector is briefly presented. The details of the analysis procedure are given in section 3 and a discussion of the cross-section measurements is presented in section 4. The final section provides a summary of the results.

2 Experimental apparatus

A detailed description of the H1 detector can be found elsewhere [1]. Here only the components relevant for this measurement are briefly described. H1 uses a coordinate system whose origin is defined by the nominal interaction point. The forward $+z$ direction denotes the direction of the incident proton beam.

The tracking system was used to reconstruct the interaction vertex and to complement the measurement of hadronic energy flow. It consists of a central part with a polar angle coverage of $25^\circ \leq \theta \leq 155^\circ$, and a forward part with a polar angle coverage of $7^\circ \leq \theta \leq 25^\circ$. The transverse momentum of charged particles was reconstructed from the curvature of tracks due to the homogeneous magnetic field of 1.15 Tesla along the beam direction, with a resolution

[1] Pseudorapidity is defined as $\eta \equiv -\ln(\tan\ \theta/2)$ where θ is the polar angle with respect to the proton direction.

$\sigma(p_T)/p_T \approx 0.6\%.p_T$/(GeV/$c$) in the central part, and $\sigma(p_T)/p_T \approx 2\%.p_T$/(GeV/$c$) in the forward part.

Events were triggered using energy deposition in a finely grained Liquid Argon (LAr) calorimeter. The LAr calorimeter covers the range in polar angle $4^\circ \leq \theta \leq 154^\circ$, with full azimuthal acceptance. It consists of an electromagnetic section with lead as an absorber, and a hadronic section with steel as an absorber. The total depth of the calorimeter ranges from 4.5 to 8 hadronic interaction lengths. The energy resolution determined in test beam measurements is $\sigma(E)/E \approx 12\ \%/\sqrt{E/\text{GeV}} \oplus 1\ \%$ for electrons and $\sigma(E)/E \approx 50\ \%/\sqrt{E/\text{GeV}} \oplus 2\ \%$ for charged pions. The absolute hadronic energy scale is presently known to $4\ \%$.

The polar region $153^\circ \leq \theta \leq 177.8^\circ$ is covered by the SPACAL, a lead/scintillating-fibre calorimeter with both electromagnetic and hadronic sections. The energy resolution for electrons is $\sigma(E)/E \approx 7.5\ \%/\sqrt{E/\text{GeV}} \oplus 2.5\ \%$, the energy resolution for hadrons is $\sigma(E)/E \approx 30\ \%/\sqrt{E/\text{GeV}}$.

The luminosity determination is based on the measurement of the Bethe-Heitler process $e^+p \rightarrow e^+\gamma p$, where the positron and the photon are detected in crystal Cherenkov calorimeters located downstream of the interaction point. The uncertainty on the measured integrated luminosity is $1.5\ \%$.

3 Analysis method

The inclusive jet sample was defined by keeping all events for which at least one jet with a transverse energy greater than 21 GeV in the pseudorapidity region $-1 \leq \eta^{jet} \leq 2.5$ was reconstructed. The jet search was performed in the laboratory frame by applying the inclusive k_T cluster algorithm [2] to all "objects" in the final state. Combined objects were defined using calorimeter clusters complemented by tracks measured in the tracking system.

The inelasticity variable y is reconstructed following the method of Jacquet and Blondel [3] from the energies and longitudinal momenta of all objects in the final state. The event sample is restricted to the kinematic region $0.1 \leq y \leq 0.9$, corresponding to a photon-proton centre-of-mass energy W ($W = \sqrt{ys}$, where s is the squared e^+p centre-of-mass energy) between 95 and 285 GeV.

The contamination from beam-gas background was reduced to a negligible level by demanding a well-reconstructed vertex in the interaction region. Cosmic shower and halo muon backgrounds were then rejected by using a set of topological muon finders in addition to the requirement that the missing transverse momentum is small compared to the total transverse energy of the events: $\not{P}_T/\sqrt{E_T} \leq (2.5\ \text{GeV})^{\frac{1}{2}}$. At this stage of the selection, the overall non ep background was estimated to correspond to less than $1\ \%$ of the data sample.

Neutral current deep inelastic scattering background was removed by rejecting all events with an identified scattered positron in the LAr calorimeter or in the SPACAL. Inefficiencies of the positron identification algorithm were compensated for, by further rejection of events with a jet having either a high proportion of electromagnetic energy or a hot core, and containing exactly one track pointing to a ϕ crack in the LAr calorimeter.

The resulting event sample consists of $17\,460$ jets reconstructed in $13\,389$ events. The γp purity of the sample was estimated to be $\sim 99\ \%$. The selection limits the virtuality of the incoming photon to the range $Q^2 < 1\ \mathrm{GeV}^2$.

Samples of direct and resolved photoproduction events were simulated using the PYTHIA 5.7 [4] and HERWIG 5.9 [5] Monte Carlo generators. The generated events were passed through a simulation [6] of the H1 detector, and reconstructed under the same conditions as the data. Hard parton-parton interactions are generated by PYTHIA and HERWIG using LO QCD matrix elements. The hard parton-parton cross-section diverges towards low $\hat{p}_t$ values[2], and therefore needs regularisation to normalise to the measured total cross-section. This is done by the introduction of a lower cut-off $\hat{p}_t^{min}$. Both generators use initial and final state parton showers to simulate higher order QCD radiation effects. The hadronisation process is performed using the Lund string model [8] as implemented in JETSET [9] in the case of PYTHIA, and using a cluster model [10] in the case of HERWIG. GRV-LO [7] parameterisations of the proton and the photon PDF were used. Multiple interactions were generated in addition to the primary parton-parton scattering. Within PYTHIA, these are calculated as LO QCD processes between partons from the proton and photon remnants and result as additional final state partons which are required to have transverse momenta of at least $1.2\ \mathrm{GeV}$. Soft particles accompanying the hard sub-process are produced in HERWIG using a soft underlying event (SUE) mechanism which includes parameterisations of experimental results on soft hadron-hadron collisions. As shown in figure 1, a reasonable description of the observed energy flow around the jet axis is obtained with both PYTHIA and HERWIG. For the latter, $35\ \%$ of the resolved interactions were generated with an additional SUE. This corresponds to an increase of the cross-section of $\sim 10\ \%$ at large η^{jet} and low E_T^{jet}. The effects of SUEs are negligible at the highest E_T^{jet}.

The HERWIG and PYTHIA Monte Carlo samples have been used to correct the data for the inefficiencies of the selection criteria and for migrations caused by detector effects. Correction factors were calculated for each bin of each distribution as the ratio $\mathcal{P}/\mathcal{E}$. The purity $\mathcal{P}$ (resp. efficiency $\mathcal{E}$) of a given bin is defined as the number of jets which enter this bin on both hadron level and reconstructed level (i.e. after detector smearing and all experimental selections) divided by the number of jets reconstructed (resp. generated) in this bin. For all measured cross-sections, bin purities and efficiencies were required to be greater than $40\ \%$. The mean values of the correction factors calculated with PYTHIA and HERWIG were used to correct bin-by-bin the data to the hadron level. The final correction factors lie between 0.9 and 1.6.

The following sources of systematic errors have been taken into account :

- the 4% uncertainty in the absolute hadronic energy scale of the LAr calorimeter leads to an uncertainty at the level of 15 to $20\ \%$ on the measurements, which is the dominant experimental uncertainty,
- the model dependency of the bin-by-bin correction leads to an error of $\sim 10\ \%$ as estimated from the difference between correction factors calculated with PYTHIA and HERWIG,

[2] $\hat{p}_t$ corresponds to the transverse momentum of the two outgoing partons in the parton-parton centre-of-mass frame.

Figure 1: Transverse energy flow integrated over $|\Delta\eta| \leq 1$ around the jet axis as a function of $\Delta\phi$ in different ranges of pseudorapidity and jet transverse energy.

- the trigger efficiency is known with an uncertainty of $5\ \%$,
- the uncertainty in the luminosity determination for this data sample is $1.5\ \%$.

4 Results

In this section, the measured differential cross-sections are presented and compared with NLO QCD calculations [14] based on the substraction method. The CTEQ5M [15] parameterisation of the proton PDF was used for the calculations. The value of Λ_{QCD} was chosen to match that of this set of PDF ($\Lambda_{QCD} = 226\ \mathrm{MeV}$ for five quark flavours, corresponding to $\alpha_s(M_Z) = 0.118$). GRV-HO [7] was chosen as the standard parameterisation of the photon PDF for this analysis. AFG-HO [16] and GSG-HO [17] were also used for comparison. The renormalisation and factorisation scales were set to $\mu_R = \mu_F = 1/2 \sum E_T^{parton}$. These scales were varied by a factor of 2 up and down in order to estimate the uncertainty corresponding to the missing higher-order terms.

Since the NLO QCD calculations refer to jets of partons, whereas the measurements refer to jets of hadrons, the predicted cross-sections have been further corrected to the hadron level. These

corrections, which do not exceed $10\ \%$, were calculated by taking the average of the ratios of cross-sections at the hadron and parton levels as given by PYTHIA and HERWIG.

The measured differential e^+p cross-section $d\sigma/dE_T^{jet}$ for inclusive jet production integrated over $-1 \leq \eta^{jet} \leq 2.5$ in the kinematic region defined by $Q^2 \leq 1\ \mathrm{GeV}^2$ and $95 \leq W \leq 285\ \mathrm{GeV}$ is shown in figure 2. The cross-section falls off by three orders of magnitude in the E_T^{jet} range between $21\ \mathrm{GeV}$ and $75\ \mathrm{GeV}$. The data are compared with QCD calculations, both at LO and NLO. Hadronisation results in a decrease of $\sim 5\ \%$ of the calculated parton-level cross-section; this hadronisation correction is roughly constant with E_T^{jet}. The NLO QCD prediction including this effect is shown in the figure together with its theoretical uncertainty, originating from the scale dependence. The fractional difference between the data and the QCD prediction is shown in figure 3. The experimental uncertainty due to the absolute energy scale of the jets, which dominates the systematic errors, is displayed as a shaded band. As shown in this figure, the calculated cross-section using the GRV-HO photon PDF is typically 5 to $10\ \%$ larger than those obtained with AFG-HO and GSG-HO. Within the errors, NLO QCD calculations describe the magnitude and the shape of the measured inclusive E_T^{jet} spectrum very well, up to the highest measured E_T^{jet} values.

The evolution of $d\sigma/dE_T^{jet}$ with y is shown in figure 4. The two y intervals presented here correspond to photon-proton centre-of-mass energies in the ranges $95 \leq W \leq 212\ \mathrm{GeV}$ and $212 \leq W \leq 285\ \mathrm{GeV}$. The E_T^{jet} spectrum at high y is harder and extends to higher E_T^{jet} values than the spectrum at low y, as expected from the higher centre-of-mass energy available. Both spectra are well reproduced by NLO QCD.

The measured differential e^+p cross-section $d\sigma/d\eta^{jet}$ for inclusive jet production integrated over $21 \leq E_T^{jet} \leq 75\ \mathrm{GeV}$ in the kinematic region defined by $Q^2 \leq 1\ \mathrm{GeV}^2$ and $95 \leq W \leq 285\ \mathrm{GeV}$ is shown in figure 5 and compared with theory in figure 6. The calculated cross-section using the GRV-HO photon PDF gives a fair description of the data while calculations using AFG-HO and GSG-HO lie slightly below the data at low η^{jet}. In figure 7 the measurement is presented in three different intervals of E_T^{jet}. The hadronisation corrections correspond to an increase (resp. decrease) of the pure partonic prediction in the forward (resp. backward) region. They tend to improve the agreement of the NLO calculations with the data, although only in a marginally significant way. Within the errors, the data are well described by the NLO QCD prediction using the GRV-HO photon PDF.

The fraction of the energy of the photon taken by the interacting parton x_γ can be reconstructed at the parton level as $x_\gamma = (\sum_{partons} E_T\ e^{-\eta})/2yE_e$. According to this formula, differences in photon PDFs, which result in differences in x_γ distributions, should reflect mostly in the η^{jet} distributions, for restricted ranges of y and E_T^{jet}. The data sample is thus separated into different y and E_T^{jet} regions, to try to discriminate between the various photon PDFs more efficiently than with the inclusive measurements alone. Measurements of $d\sigma/d\eta^{jet}$, in two regions of y and three intervals of E_T^{jet}, are presented in figure 8. The maximum of the cross-section is shifted towards low η^{jet} values when increasing y. This is expected since, in the laboratory frame, this corresponds to an increased boost of the events in the backward direction. NLO QCD predictions are in general in good agreement with the measured cross-sections. The only distribution which gives some sensitivity to the different photon PDFs is the one in the highest y and lowest η^{jet} region. Here, the GRV-HO photon PDF gives the best description of the data; however, the precision of the experimental measurement (as well as the theoretical uncertainty

not presented in figure 8) does not allow any firm conclusion on which PDF is favoured by data to be drawn.

In order to compare with a previous ZEUS measurement [11], the kinematic range has been reduced to $0.2 \leq y \leq 0.85$ and $-0.75 \leq \eta^{jet} \leq 2.5$. Figure 9 shows the differential e^+p cross-section $d\sigma/dE_T^{jet}$ measured by H1 for this restricted range, compared with the ZEUS preliminary result. The inner error bars of the H1 data represent the statistical errors, the outer show the quadratic sum of statistical and systematic uncertainties. Within the errors, the two measurements are in good agreement.

To compare with another ZEUS measurement [13] of the inclusive η^{jet} spectrum, the complete analysis chain described in section 3 has been re-done using an iterative cone algorithm [12] with a radius $R = 1$ in the (η, ϕ) plane. The resulting differential e^+p cross-sections $d\sigma/d\eta^{jet}$ integrated for E_T^{jet} above two different thresholds ($E_T^{jet} \geq 21$ and 25 GeV) are shown in figure 10. Again there is no significant difference between the measurements from both experiments.

5 Summary

A new measurement of inclusive high E_T jet production cross-sections in quasi-real photoproduction ($Q^2 \leq 1$ GeV^2) ep interactions has been presented, based on $\mathcal{L} = 24$ pb^{-1} of e^+p data collected by H1 in 1996-1997. The kinematic range of the measurement corresponds to photon-proton centre-of-mass energies $95 \leq W \leq 285$ GeV. The jets were found in the pseudorapidity range $-1 \leq \eta^{jet} \leq 2.5$ using the inclusive k_T algorithm in the laboratory frame and were required to have transverse energy in the interval $21 < E_T^{jet} < 75$ GeV. Measured cross-sections were corrected to the hadron level, and compared to NLO QCD calculations, with or without hadronisation corrections. Within the experimental and theoretical uncertainties, the measured distributions are well described, both in normalisation and shape, by NLO QCD calculations using various available photon PDFs, even without hadronisation corrections. The hadronisation corrections to the NLO QCD calculations only slightly improve the agreement with the data. The current precision of the experimental results as well as the theoretical predictions do not allow discrimination between the different photon PDFs. Data are in agreement with previously presented ZEUS results.

Acknowledgements

We are grateful to the HERA machine group whose outstanding efforts have made and continue to make this experiment possible. We thank the engineers and technicians for their work in constructing and now maintaining the H1 detector, our funding agencies for financial support, the DESY technical staff for continual assistance, and the DESY directorate for the hospitality which they extend to the non DESY members of the collaboration.

References

[1] H1 Collab., I. Abt et al., Nucl. Instr. and Meth. A386 (1997) 310; 348.

[2] S.D. Ellis and D.E. Soper, Phys. Rev. D48 (1993) 3160.

[3] A. Blondel and F. Jacquet,
Proceedings of the Study of an ep Facility for Europe,
ed. U. Amaldi, DESY 79/48 (1979) 391.

[4] T. Sjöstrand, CERN-TH-6488 (1992), Comput. Phys. Commun. 82 (1994) 74.

[5] G. Marchesini et al., Comp. Phys. Commun. 67 (1992) 465.

[6] R. Brun et al., CERN DD/EE/84-1 (1987).

[7] M. Glück, E. Reya and A. Vogt, Phys. Rev. D46 (1992) 1973.

[8] B. Andersson et al., Phys. Rep. 97 (1983) 31.

[9] T. Sjöstrand, Comput. Phys. Commun. 39 (1986) 347;
T. Sjöstrand, M. Bengtsson, Comput. Phys. Commun. 43 (1987) 367.

[10] B.R. Webber, Nucl. Phys. B238 (1984) 192.

[11] ZEUS Collab., Inclusive jet photoproduction at HERA,
Prepared for 29th International Conference on High-Energy Physics (ICHEP 98),
Vancouver, Canada, 23-29 July 1998.

[12] L.A. del Pozo, PhD Thesis, University of Cambridge,
Cambridge, England (1993) RALT-002.

[13] ZEUS Collab., J. Breitweg et al., Eur. Phys. J. C4 (1998) 591.

[14] S. Frixione, G. Ridolfi, Nucl. Phys. B507 (1997) 315.

[15] H.L. Lai et al., Eur. Phys. J. C12 (2000) 375.

[16] P. Aurenche et al., Z. Phys. C56 (1992) 589.

[17] L.E. Gordon and J.K. Storrow, Z. Phys. C56 (1992) 307.

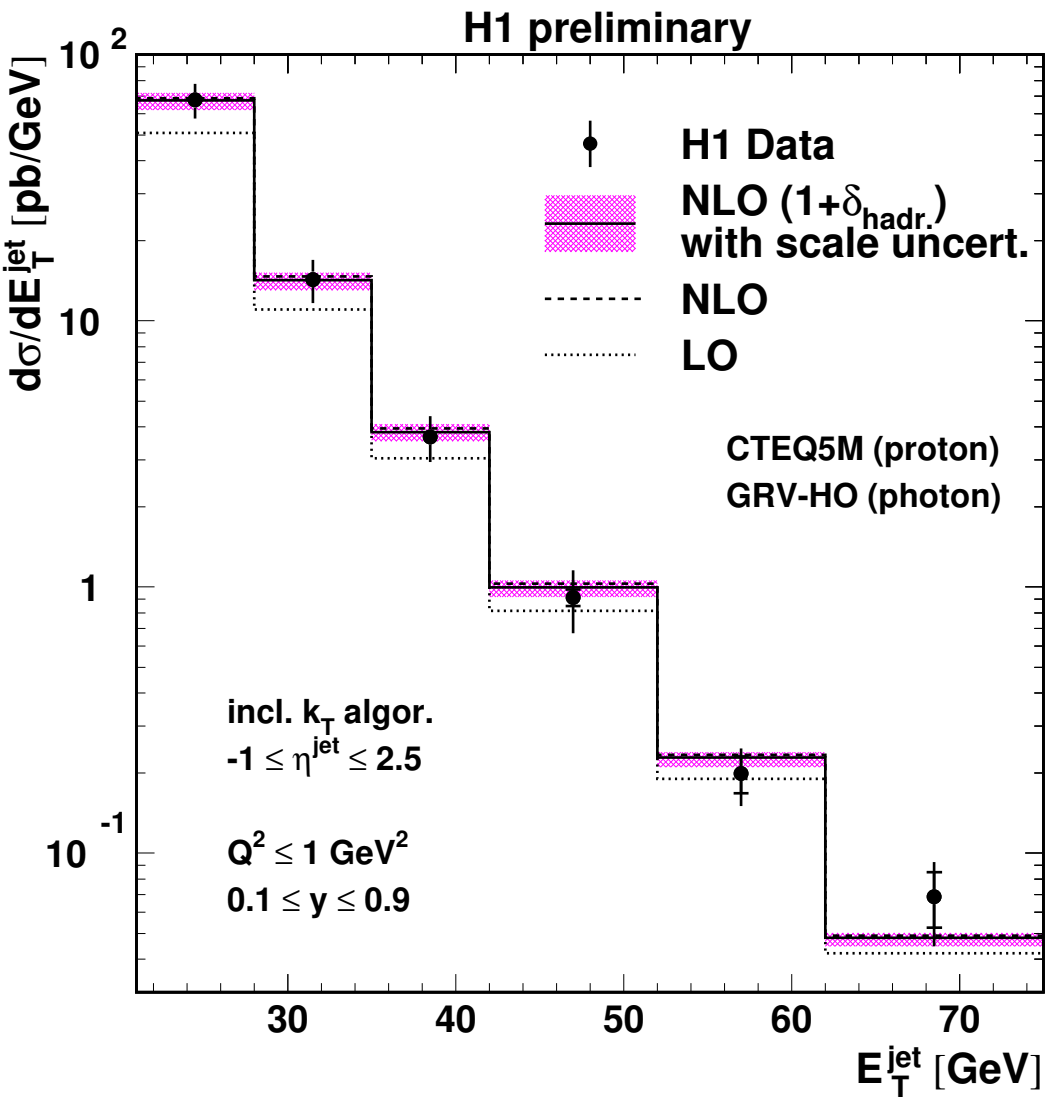

Figure 2: The measured differential e^+p cross-section $d\sigma/dE_T^{jet}$ for inclusive jet production using the inclusive k_T algorithm integrated over $-1 \leq \eta^{jet} \leq 2.5$ in the kinematic region defined by $Q^2 \leq 1$ GeV^2 and $0.1 \leq y \leq 0.9$. The inner error bars represent the statistical errors of the data, and the outer show the statistical and systematic uncertainties added in quadrature. Data are compared with QCD calculations using GRV-HO photon parton distributions and CTEQ5M proton parton distributions. The LO and NLO predictions are shown as dotted and dashed lines respectively. The full line indicates the NLO predictions with hadronisation corrections. The renormalisation and factorisation scales are defined by $\mu_R = \mu_F = \sum E_T/2$. The hatched band displays the uncertainty on the NLO QCD predictions obtained by varying the renormalisation and factorisation scales by a factor of 2 up and down.

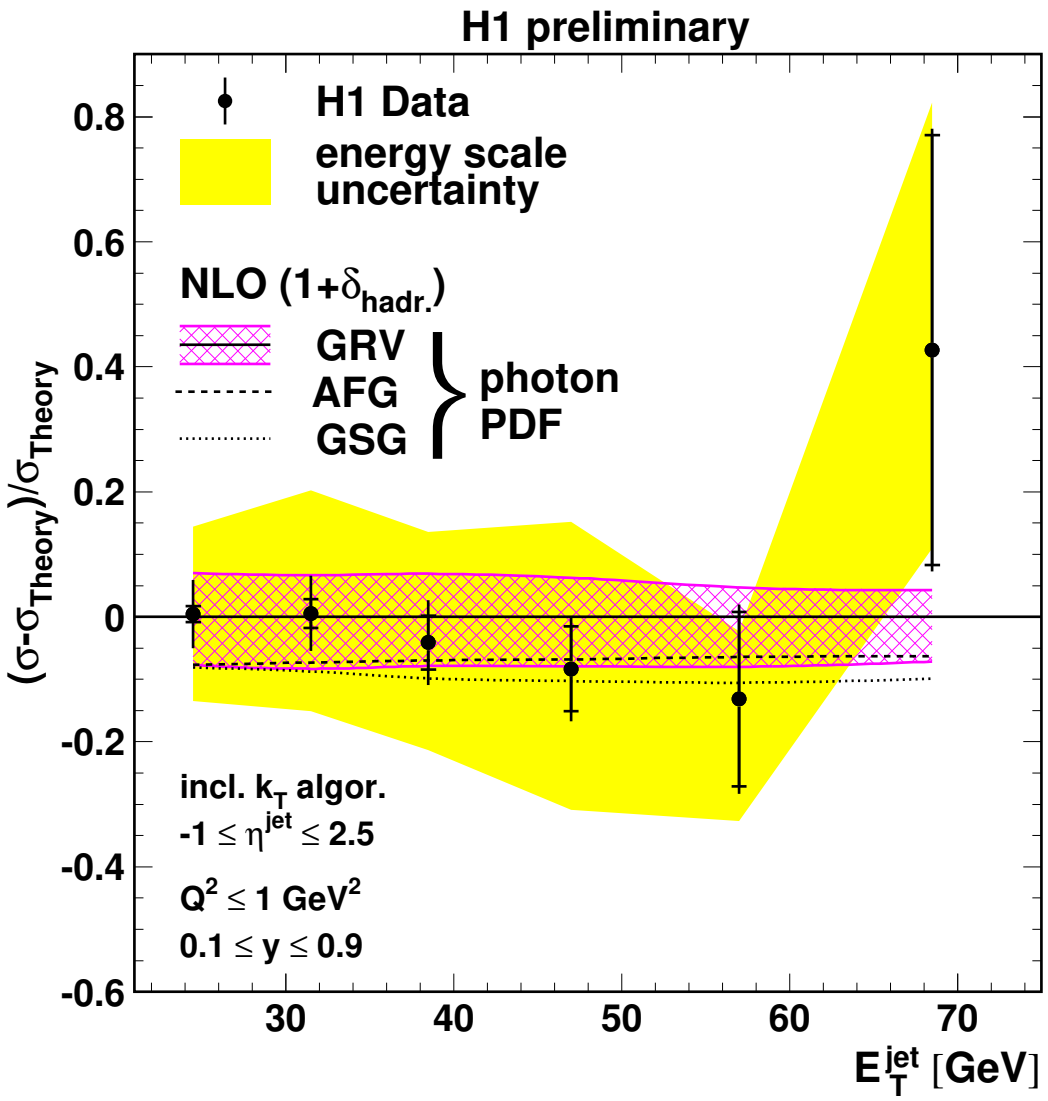

Figure 3: The relative difference between the measured differential e^+p cross-section $d\sigma/dE_T^{jet}$ for inclusive jet production using the inclusive k_T algo rithm integrated over $-1 \leq \eta^{jet} \leq 2.5$ in the kinematic region defined by $Q^2 \leq 1$ GeV^2 and $0.1 \leq y \leq 0.9$, and the NLO calculation based on GRV-HO and CTEQ5M parameterisations of the photon and proton parton densities, including hadronisation corrections. The inner error bars represent the statistical errors of the data, and the outer show the statistical and systematic uncertainties added in quadrature, except for the uncertainty associated with the absolute energy scale of the jets, which is shown separately as a shaded band. Comparisons of the NLO QCD calculation usi ng GRV-HO photon parton distributions with those using AFG-HO and GSG-HO photon parton distributions are shown as dashed and dotted lines respectively. The renormalisation and factorisation scales are defined by $\mu_R = \mu_F = \sum E_T/2$. The hatched band displays the uncertainty on the NLO QCD prediction s obtained by varying the renormalisation and factorisation scales by a factor of 2 up and down.

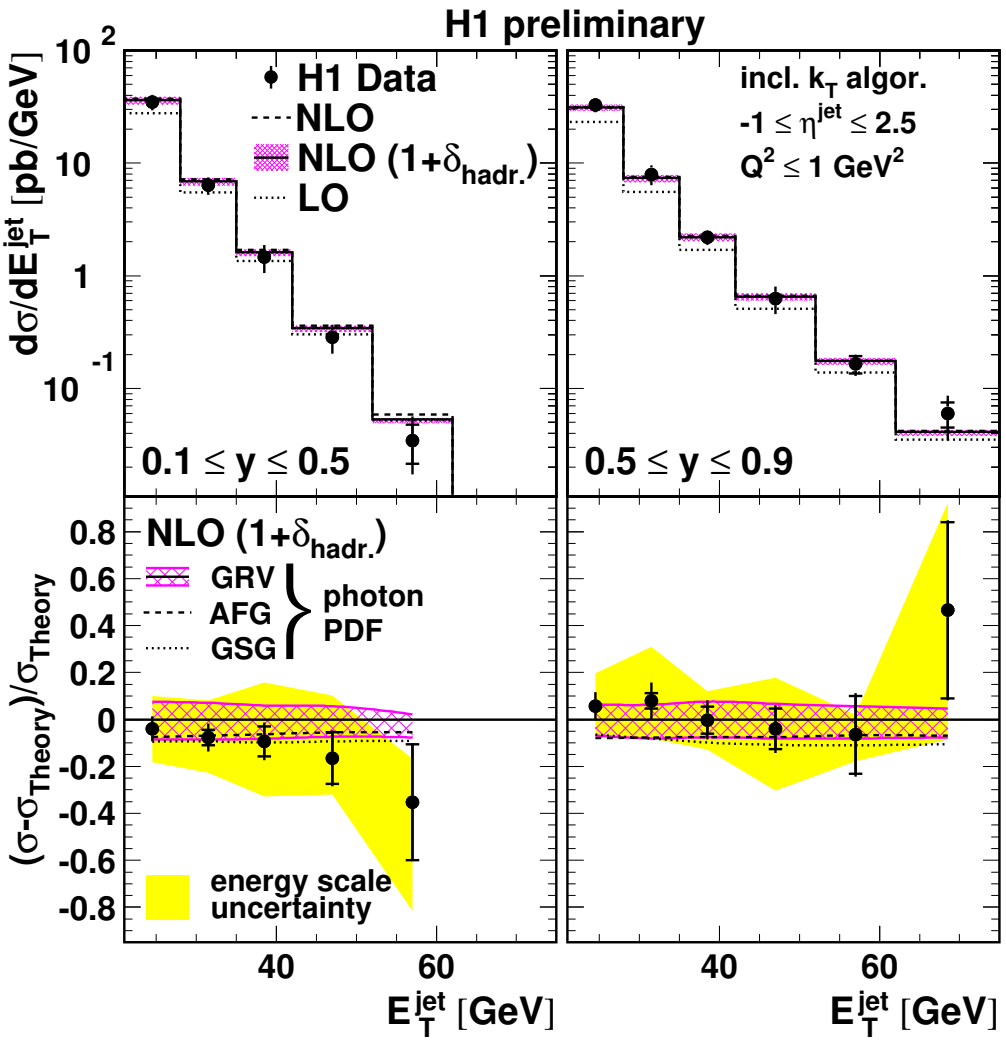

Figure 4: The measured differential e^+p cross-section $d\sigma/dE_T^{jet}$ for inclusive jet production at $Q^2 \leq 1$ GeV^2 using the inclusive k_T algorithm integrated over $-1 \leq \eta^{jet} \leq 2.5$ for $0.1 \leq y \leq 0.5$ (upper left plot) and $0.5 \leq y \leq 0.9$ (upper right plot). The inner error bars represent the statistical errors of the data, and the outer show the statistical and systematic uncertainties added in quadrature. Data are compared with QCD calculations using GRV-HO and CTEQ5M parton distributions for the photon and the proton. The LO and NLO predictions are shown as dotted and dashed lines respectively. The full line indicates the NLO predictions with hadronisation corrections. The renormalisation and factorisation scales are defin ed by $\mu_R = \mu_F = \sum E_T/2$. The hatched band displays the uncertainty on th e NLO QCD predictions obtained by varying the renormalisation and factorisation scales by a factor of 2 up and down. The relative difference between the data and the NLO calculation based on GRV-HO and CTEQ5M is shown on the two lower plots. The inner error bars represent the statistical errors of the data, and the outer show the statistical and systematic uncertainties added in quadrature, except for the uncertainty associated with the absolute energy scale of the jets, which is shown separately as a shaded band. Comparisons of the NLO QCD calculations using GRV-HO with those using AFG-HO and GSG-HO photon parton distributions are shown as dashed and dotted lines respectively.

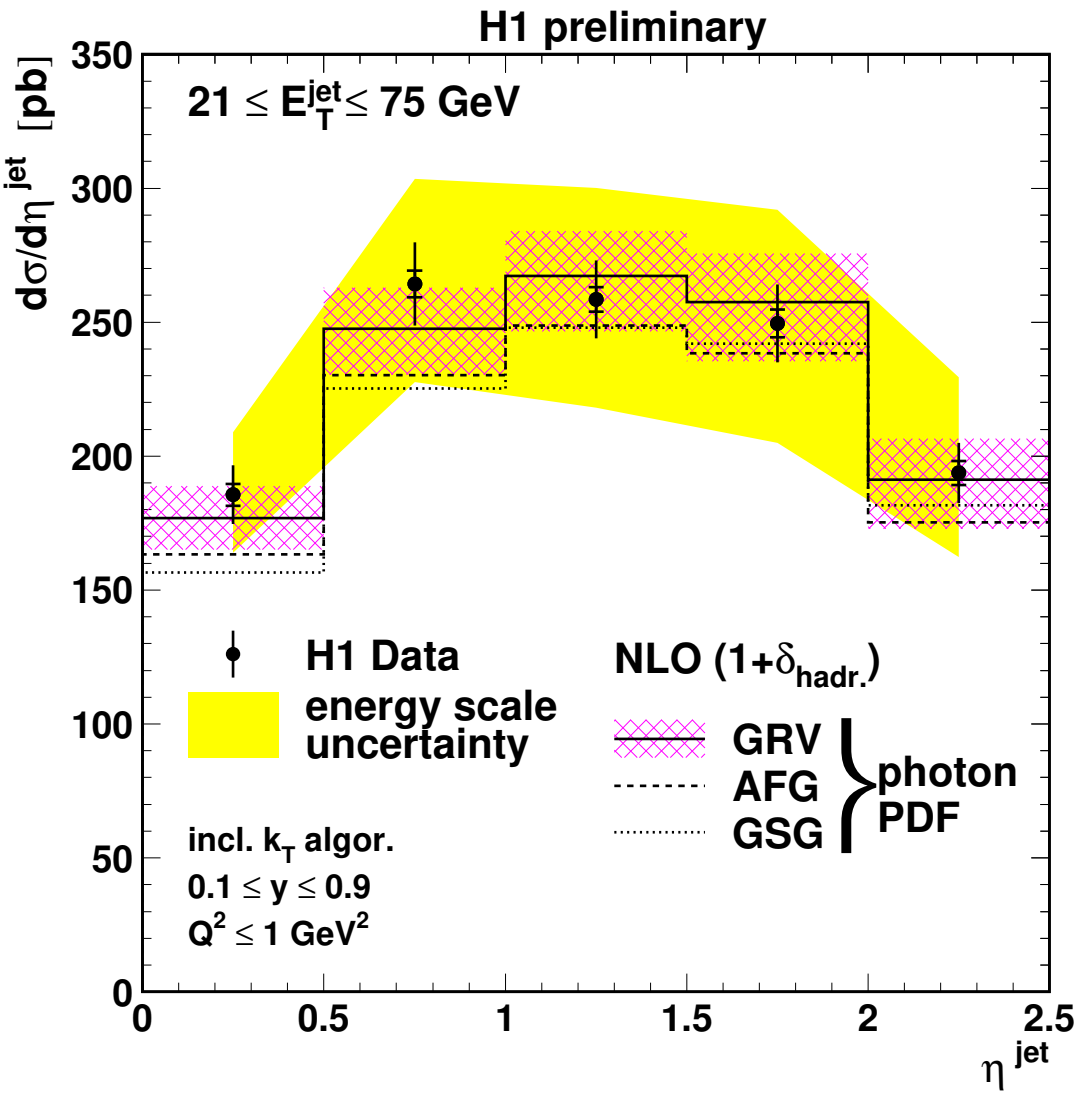

Figure 5: The measured differential e^+p cross-section $d\sigma/d\eta^{jet}$ for inclusive jet production using the inclusive k_T algorithm integrated over $21 \leq E_T^{jet} \leq 75$ GeV in the kinematic region defined by $Q^2 \leq 1$ GeV^2 and $0.1 \leq y \leq 0.9$. The inner error bars represent the statistical errors of the data, and the outer show the statistical and systematic uncertainties added in quadrature, except for the uncertainty associated with the absolute energy scale of the jets, which is shown separately as a shaded band. Data are compared with NLO QCD predictions taking into account hadronisation corrections obtained by using GRV-HO (full line), AFG-HO (dashed line) and GSG-HO (dotted line) photon parton distributions and CTEQ5M proton parton distributions. The renormalisation and factorisation scales are defined by $\mu_R = \mu_F = \sum E_T/2$. The hatched band displays the uncertainty on the NLO QCD prediction s using GRV-HO photon parton distributions obtained by varying the renormalisation and factorisation scales by a factor of 2 up and down.

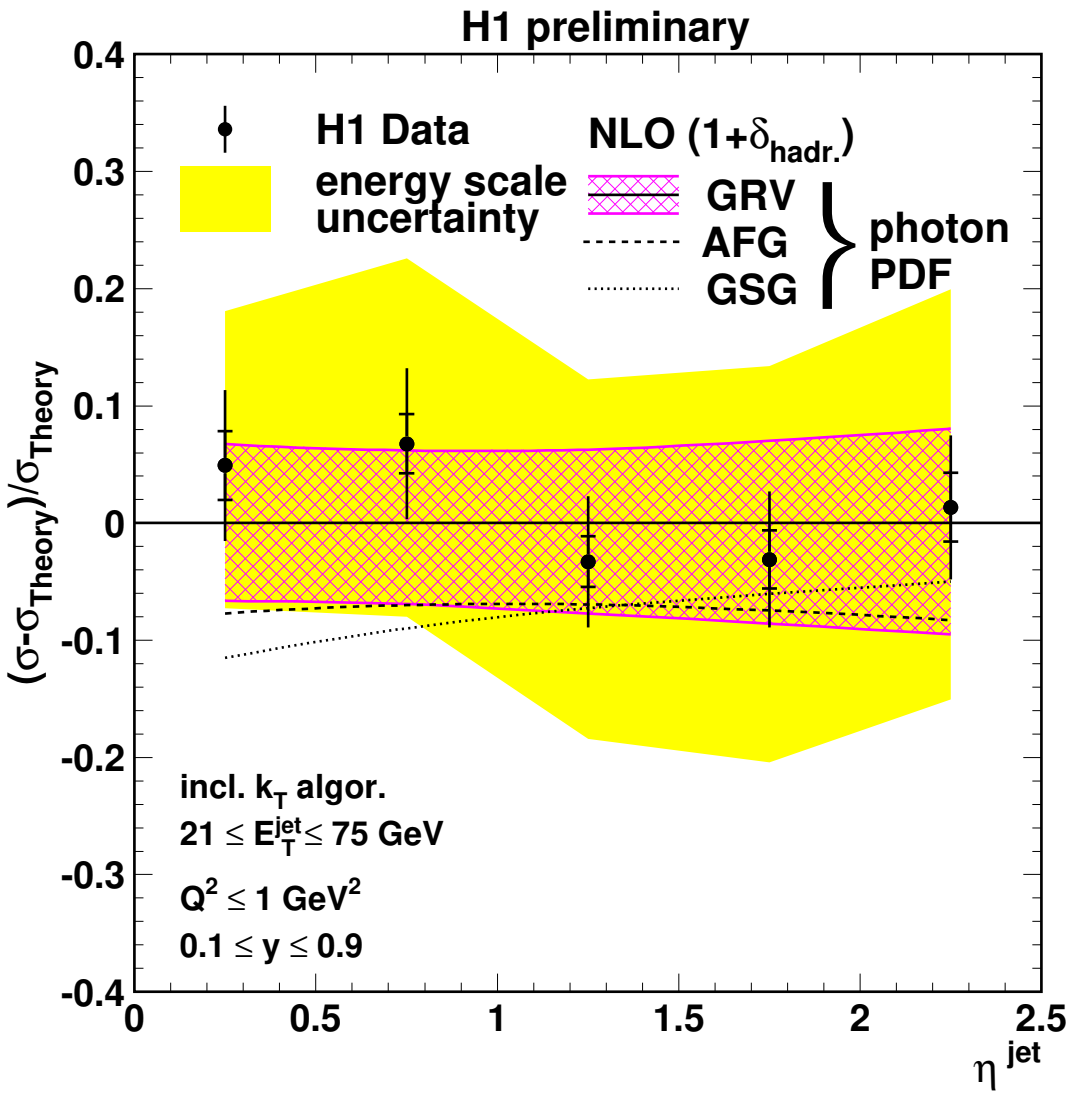

Figure 6: The relative difference between the measured differential e^+p cross-section $d\sigma/d\eta^{jet}$ for inclusive jet production using the inclusive k_T alg orithm integrated over $-1 \leq \eta^{jet} \leq 2.5$ in the kinematic region defined by $Q^2 \leq 1$ GeV^2 and $0.1 \leq y \leq 0.9$, and the NLO calculation based on GRV-HO and CTEQ5M parameterisations of the photon and proton parton densities, including hadronisation corrections. The inner error bars represent the statistical errors of the data, and the outer show the statistical and systematic uncertainties added in quadrature, except for the uncertainty associated with the absolute energy scale of the jets, which is shown separately as a shaded band. Comparisons of the NLO QCD calculation using GRV-HO photon parton distributions with those using AFG-HO and GSG-HO photon parton distributions are shown as dashed and dotted lines respectively. The renormalisation and factorisation scales are defined by $\mu_R = \mu_F = \sum E_T/2$. The hatched band displays the uncertainty on the NLO QCD prediction s obtained by varying the renormalisation and factorisation scales by a factor of 2 up and down.

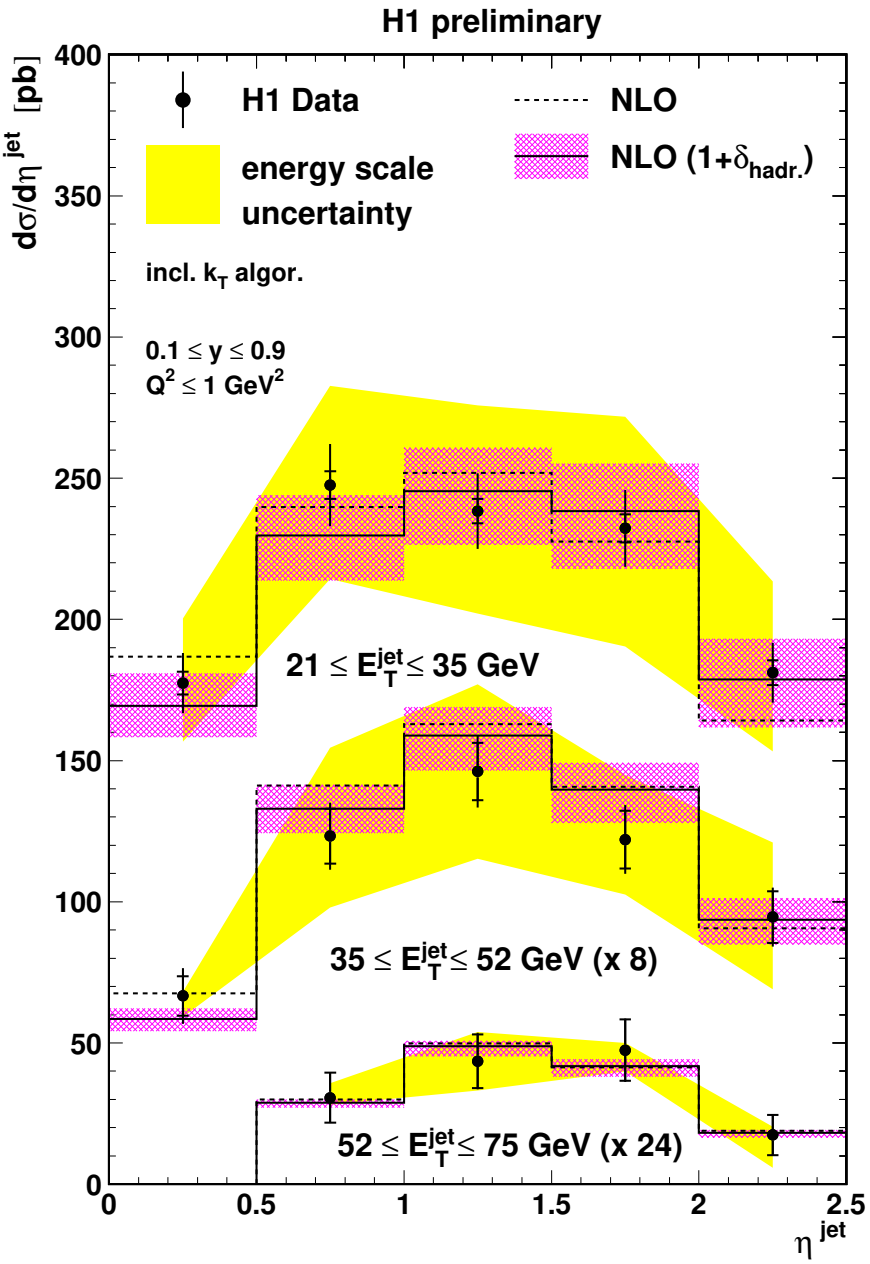

Figure 7: The measured differential e^+p cross-section $d\sigma/d\eta^{jet}$ for inclusive jet production using the inclusive k_T algorithm integrated over various E_T^{jet} ranges in the kinematic region defined by $Q^2 \leq 1\ \mathrm{GeV}^2$ and $0.1 \leq y \leq 0.9$. The inner error bars represent the statistical errors of the data, and the outer show the statistical and systematic uncertainties added in quadrature, except for the uncertainty associated with the absolute energy scale of the jets, which is shown separately as a shaded band. Data are compared with NLO QCD predictions taking into account hadronisation corrections (full line) obtained b y using GRV-HO photon parton distributions and CTEQ5M proton parton distributions. The renormalisation and factorisation scales are defined by $\mu_R = \mu_F = \sum E_T/2$. The hatched band displays the uncertainty on the NLO QC D predictions obtained by varying the renormalisation and factorisation scales by a factor of 2 up and down. The dashed line shows the NLO QCD predictions without applying hadronisation corrections.

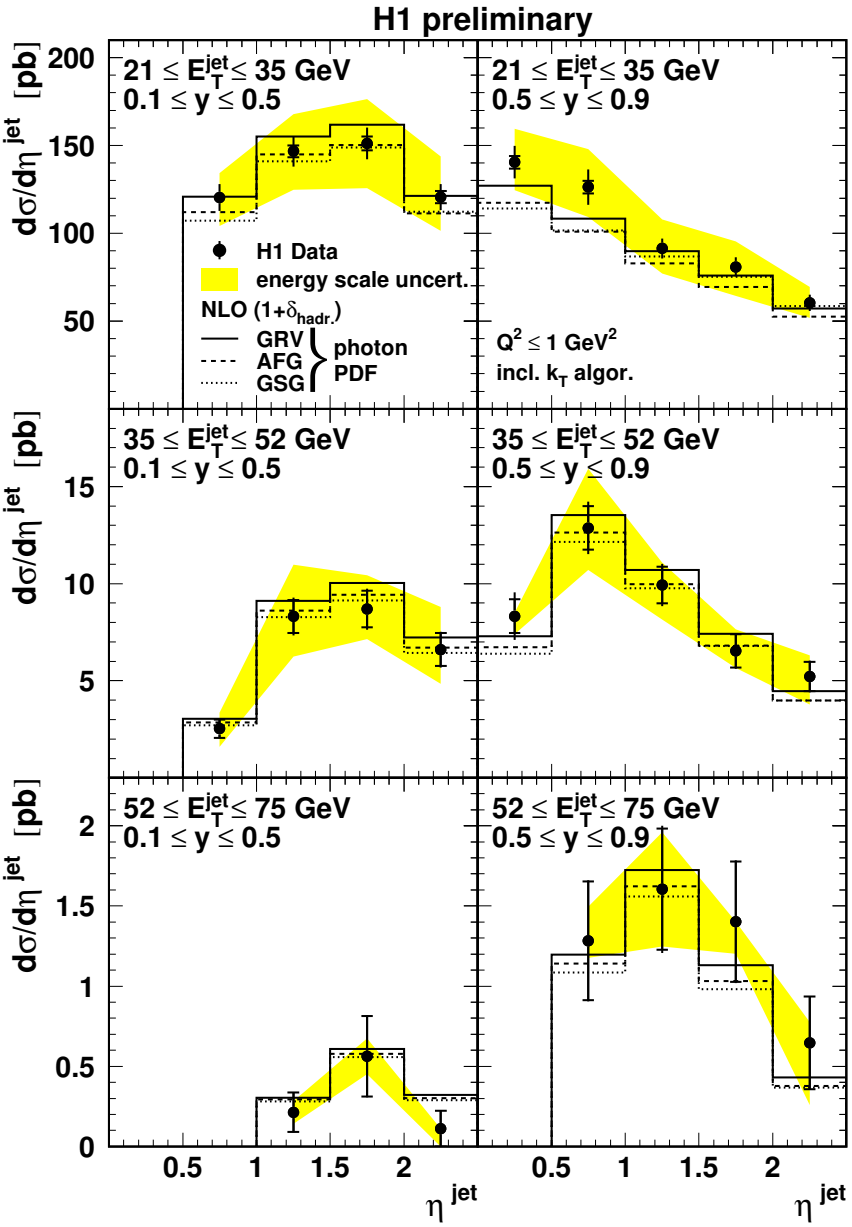

Figure 8: The measured differential e^+p cross-section $d\sigma/d\eta^{jet}$ for inclusive jet production using the inclusive k_T algorithm integrated over various E_T^{jet} and y ranges in the kinematic region defined by $Q^2 \leq 1\ \mathrm{GeV}^2$. The inner error bars represent the statistical errors of the data, and the outer show the statistical and systematic uncertainties added in quadrature, except for the uncertainty associated with the absolute energy scale of the jets, which is shown separately as a shaded band. Data are compared with NLO QCD predictions taking into account hadronisation corrections obtained by using GRV-HO (full line), AFG-HO (dashed line) and GSG-HO (dotted line) photon parton distributions and CTEQ5M proton parton distributions. The renormalisation and factorisation scales are defined by $\mu_R = \mu_F = \sum E_T/2$.

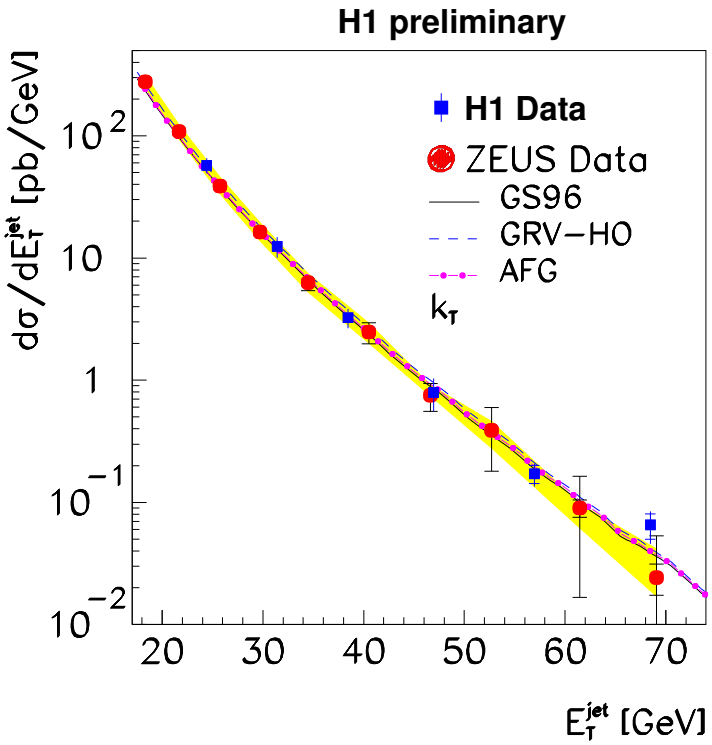

Figure 9: The differential e^+p cross-section $d\sigma/dE_T^{jet}$ for inclusive jet production using the inclusive k_T algorithm integrated over $-0.75 \leq \eta^{jet} \leq 2.5$ and $0.2 \leq y \leq 0.85$. Data are compared with the preliminary result from ZEUS [11].

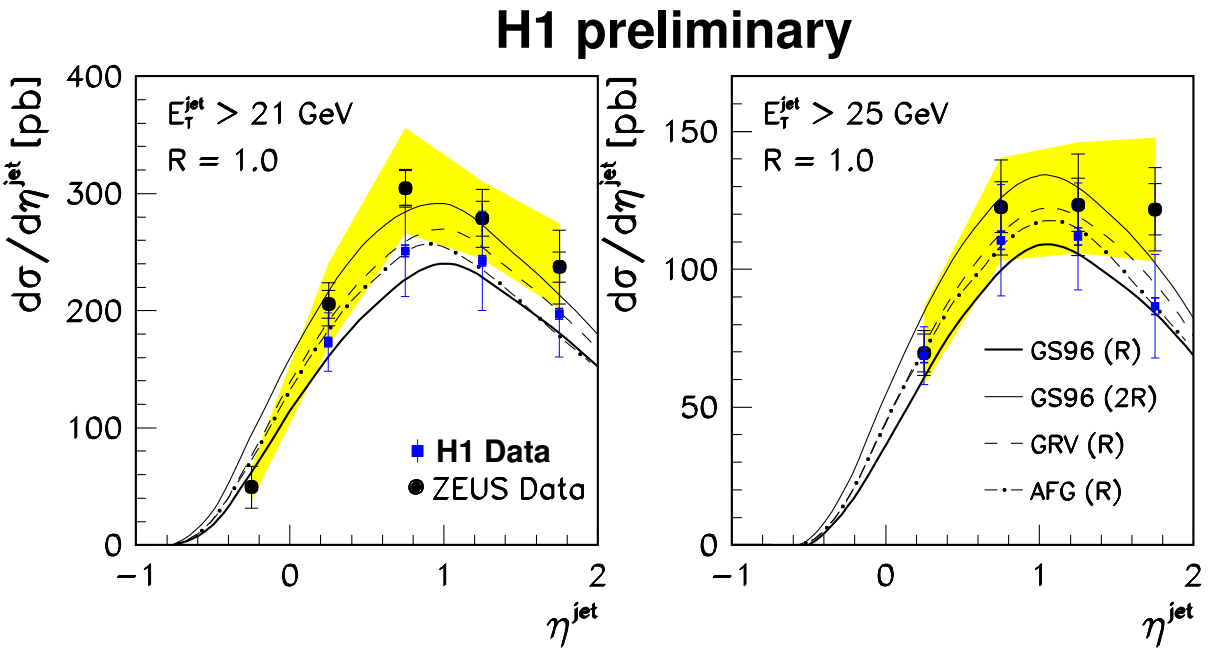

Figure 10: The differential e^+p cross-section $d\sigma/d\eta^{jet}$ for inclusive jet production using the CDF cone algorithm with radius $R = 1$ integrated over $0.2 \leq y \leq 0.85$ and $E_T^{jet} > E_0$ for two different thresholds $E_0 = 21$ G eV (left plot) and $E_0 = 25$ GeV (right plot). Data are compared with the published results from ZEUS [13].